INTERNATIONAL JOURNAL FOR NUMERICAL METHODS IN FLUIDS
Int. J. Numer. Meth. Fluids 2008; **57**:1211–1226
Published online 14 April 2008 in Wiley InterScience (www.interscience.wiley.com). DOI: 10.1002/fld.1812

Projection method for flows with large local density gradients: Application to dendritic solidification

J. C. Heinrich[1,*,†], U. K. Sajja[2], S. D. Felicelli[2] and D. G. Westra[3]

[1]*Department of Mechanical Engineering, The University of New Mexico, Albuquerque, NM 87131, U.S.A.*
[2]*Department of Mechanical Engineering, Mississippi State University, Mississippi State, MS 39762, U.S.A.*
[3]*NASA Marshall Space Flight Center, Huntsville, AL 35812, U.S.A.*

SUMMARY

Numerical models of solidification including a mushy zone are notoriously inefficient; most of them are based on formulations that require the coupled solution to the velocity components in the momentum equation greatly restricting the range of applicability of the models. Initial attempts at modeling directional solidification in the presence of a developing mushy zone using a projection formulation encountered difficulties once solidification starts, which were traced to the inability of the method to deal with large local density differences in the vicinity of the fluid–mush interface. A modified formulation of the projection method has been developed that maintains the coupling between the body force and the pressure gradient and is presented in this work. This formulation is shown to be robust and extremely efficient; reducing very significantly the necessary storage and the computational time required for the simulation of problems involving very large meshes when compared with previously published data. This is illustrated in this work through its application to simulations involving a Pb–Sn alloy. Copyright © 2008 John Wiley & Sons, Ltd.

Received 25 January 2008; Revised 21 February 2008; Accepted 25 February 2008

KEY WORDS: mushy zone model; finite elements; dendritic solidification; projection method; channel formation; three-dimensional solidification

1. INTRODUCTION

Models of solidification of alloys in the mesoscale (1–100 mm) that capture the evolution of the mushy zone in an average sense began to appear in the 1960s. Initially, these models concentrated

[*]Correspondence to: J. C. Heinrich, Department of Mechanical Engineering, The University of New Mexico, Albuquerque, NM 87131, U.S.A.
[†]E-mail: heinrich@unm.edu

Contract/grant sponsor: National Aeronautics and Space Administration
Contract/grant sponsor: National Science Foundation; contract/grant number: CTS-0553570

on the effect of solute redistribution in macrosegregation [1–9], and included only buoyancy-driven convection in the interdendritic liquid. Later on in the mid-1980s, models capable of describing macrosegregation when thermosolutal convection in the liquid is important and the geometry of the mushy zone varies with time were developed; this allowed the models to capture the formation of 'freckles' or channel segregates that evolve from the interaction of thermosolutal convection with the mushy zone and the partial remelting of the dendrites [10–14]. These models do not resolve the microstructure in the mushy zone, rather; the solid-fluid mix is treated as a porous medium and the equations are developed using volume averaging [15, 16] or mixture theory [10, 13]. This eliminates the need to model the solid–fluid interface. The fluid and mushy zones can be treated as a single domain using a momentum equation that includes a Darcy term with variable anisotropic permeability in the mushy zone, and that reduces to the standard Navier–Stokes equations in the all-liquid region. Most of the work that has been reported in the literature addresses two-dimensional calculations. References [11, 13, 14, 17–23] are some of the most representative publications but by no means a comprehensive list; literature reviews have appeared in [24–26].

All of the models cited above solve the velocity and pressure as a coupled system of equations making them computationally inefficient; this is probably one of the reasons why the activity in this area has declined significantly in recent years. It is well known that projection (or fractional step) methods [27–34] are the most efficient for the solution to the Navier–Stokes equations, but their use in solidification models has been very limited [35–37]. Moreover, in the first two of these references the authors presented modest calculations with two-dimensional meshes in the order of 30×40 elements, which can also be properly handled by coupled methods. To the authors knowledge no large calculations have been attempted. The inefficiency of the existing methods referred to the above has made it extremely expensive to apply in important practical situations where the potential development of freckles is not known *a priori* [38]; this motivated the work of Westra [37] where a projection method was developed. This particular effort aimed at obtaining a more efficient model capable of performing calculations in very large meshes at a reasonable cost. However, the work in [37] encountered significant difficulties in the implementation. Even though a method capable of performing large calculations was implemented, it was difficult to use and require modifications according to the specific problem at hand, making it impractical. These difficulties were traced to the inability of the model to capture large local density differences at the interface between the tip of the dendrites and the all-liquid region when solidification takes place, and motivated the development of the formulation presented in this work.

In this paper a finite element model is presented that is based on the projection method and formulated to maintain an implicit coupling between the body force terms and the pressure. The formulation calculates the intermediate velocities explicitly making it highly parallelizable, and it uses a stabilized Petrov–Galerkin formulation based on trilinear elements (three-dimensional). In the following section we discuss three-dimensional mushy zone models; the solidification model is presented in Section 3; the projection method is formulated in Section 4 and some aspects of the discretization are discussed in Section 5. The results of simulations are discussed in Section 6.

2. THREE-DIMENSIONAL SIMULATIONS

Considerably less work has been published on three-dimensional than two-dimensional models and simulations of dendritic solidification with a developing mushy zone; the models that have been

DOI: 10.1002/fld

published also solve the momentum equations as a coupled system [39–43]. In [39] calculations for a binary mixture of NH_4Cl-H_2O with a mass fraction of 32% NH_4Cl, in a cylinder segment of height 102 mm, radius 64 mm and a 45° angle were presented. A grid of $42\times42\times13$ points and a finite volume formulation were utilized. In the z-direction, the grid was non-uniformly graded to provide for better resolution at the bottom. The calculations required roughly 17 min CPU time per second of solidification on a Cyber 205 computer. Reference [40] presented calculations for a binary Pb–10 wt% Sn mixture in a parallelepiped of cross section $10\,\mathrm{mm}\times10\,\mathrm{mm}$ and 20 mm height and in a cylinder of 10 mm diameter and 20 mm height. A finite element method combined with a Galerkin least-squares (GLS) formulation was used. The parallelepiped was discretized with a $20\times20\times30$ element mesh of uniform trilinear elements and the cylinder with a mesh of 12,360 hexahedral isoparametric eight-node elements. A typical calculation took about 2 min CPU time per second of solidification on an SG Power Challenge utilizing one processor. Reference [41] presents an extension of the model in [40] to multi-component alloys. A calculation for a Ni-based alloy with 6 wt% Al, 6 wt% Ta and 5 wt% W was performed in a parallelepiped of 10 mm in the x-direction, 20 mm in the y-direction and 30 mm in the z-direction (height). The mesh contained $20\times40\times30$ trilinear elements in the x-, y- and z-directions, respectively. The calculation took approximately 4.2 min CPU time per second of solidification in the SG machine mentioned above. In more recent publications [42, 43], calculations for a binary Pb–10 wt% Sn alloy have been presented. In [42] the computational region was a $3\,\mathrm{mm}\times3\,\mathrm{mm}\times10\,\mathrm{mm}$ parallelepiped discretized using four-node tetrahedral finite elements. The finest mesh used contained 979 549 elements and 169 768 nodes, and required approximately 25 min CPU time per second of solidification on an HP C180 workstation with 512 MB memory. The calculation in [43] involved a parallelepiped of $10\,\mathrm{mm}\times10\,\mathrm{mm}\times20\,\mathrm{mm}$ discretized using a stabilized finite element method with a $20\times20\times30$ trilinear brick elements; no information was reported on the CPU time required for these calculations. If we consider that in the above models the meshes were primarily selected according to the storage capacity of the hardware, it is clear that the models are not suitable at the present time to perform realistic three-dimensional calculations.

Only two implementations of projection methods in three dimensions are known to the authors [37, 44]. The work in [37] has already been mentioned in the context of two dimensions, here a calculation for a Pb–10 wt% Sn alloy in a $10\,\mathrm{mm}\times10\,\mathrm{mm}\times20\,\mathrm{mm}$ parallelepiped was presented. The mesh consisted of $40\times40\times111$ trilinear elements with 188 272 nodes and required roughly 60 min of CPU time per second of solidification simulation on a Compaq GS60E. In Reference [44], the emphasis was on the model for porosity formation; it presents a calculation for a relatively complex A356 plate casting with the largest spatial dimension in the order of 20 cm. There are various simplifying assumptions in the convection model, the solution algorithm is based on SOLA and SIMPLE, and utilizes other software such as Thermo Calc and DICTRA. Unfortunately, no information is given about the meshes or the efficiency of the model. However, it is evident that the calculation would be representative of a practical engineering geometry.

The CPU times given above are those reported by the authors and have to be evaluated according to the computer hardware used at the time. All of the models would perform better if executed in today's faster machines. In [45], evidence was presented supporting the hypothesis that the number of computational nodes used in simulations of solidification processes has doubled every 18 months during the last 30 years, and in the year 2000, calculations with 10^8 nodes were reported [45]. This trend appears to hold for models that, in general, consider fluid flow and heat transfer in the mold filling and cooling process. However, this hypothesis has not been realized for the mushy zone models discussed here. Starting in 1984, the lower bound given in figure 2 of [45]

DOI: 10.1002/fld

predicts calculations using 10^7 nodes today. Nevertheless, the largest calculations reported so far (even in this work) do not go beyond $O(10^5)$ nodes. The scheme proposed in this work will allow us to bring mushy zone simulations up to par with other areas of solidification modeling.

3. SOLIDIFICATION MODEL

Let us consider the solidification of a binary alloy. The basic assumptions are Darcy type, laminar, incompressible and Newtonian flow with anisotropic permeability in the mushy zone; no pore formation, only solid and liquid phases; stationary solid and no diffusion in the solid; density that can be different in the solid and liquid, but constant within each phase; the specific heat in the solid and liquid can be different but all other properties are equal and constant in both phases. The assumptions of constant properties in each phase simplify the model considerably but are not necessary; the formulation using fully variable properties, including in particular the density and specific heat was presented in [46]. The continuum equations of continuity, momentum, energy and solute conservation can be developed using volume averaging [15, 16], the first two of these are

$$\nabla\cdot\rho_\mathrm{l}\mathbf{u}=(\rho_\mathrm{S}-\rho_\mathrm{l})\frac{\partial\phi}{\partial t} \tag{1}$$

$$\begin{aligned}\frac{\partial\mathbf{u}}{\partial t}+\frac{\mathbf{u}}{\phi}\cdot\nabla\mathbf{u}-\frac{(\rho_\mathrm{S}-\rho_\mathrm{l})}{\rho_\mathrm{l}\phi}\frac{\partial\phi}{\partial t}\mathbf{u}=-\frac{\phi}{\rho_\mathrm{l}}\nabla p+v\left[\nabla^2\mathbf{u}+\frac{(\rho_\mathrm{S}-\rho_\mathrm{l})}{3\rho_\mathrm{l}}\nabla\frac{\partial\phi}{\partial t}\right]\\ -v\phi\mathbf{K}^{-\mathbf{1}}\mathbf{u}+\frac{\rho\phi}{\rho_\mathrm{l}}\mathbf{g}\end{aligned} \tag{2}$$

where ρ_l is the density of the liquid, ρ_S the density of the solid, $\mathbf{u}$ the superficial velocity, ϕ the volume fraction of liquid and t the time. In Equation (2) p is the pressure, v the kinematic viscosity, $\mathbf{K}$ the permeability, $\mathbf{g}$ the gravitational force and ρ denotes the variable density in the body forces using the Boussinesq approximation, which in this work assumes the form

$$\rho=\rho_\mathrm{l}[1+\beta_\mathrm{T}(T-T_0)+\beta_\mathrm{C}(S_\mathrm{l}-S_0)] \tag{3}$$

Here β_T and β_C are the thermal and solutal coefficients of volumetric expansion, respectively, S_l is the solute concentration in the liquid, and T_0 and S_0 are the reference temperature and solute concentrations at which ρ_l is given.

The energy and solute conservation equations are

$$\overline{\rho c}_p\frac{\partial T}{\partial t}+\rho_\mathrm{S}[(c_{p\mathrm{S}}-c_{p\mathrm{l}})(T_\mathrm{H}-T)+L]\frac{\partial\phi}{\partial t}+\rho_\mathrm{l}c_{p\mathrm{l}}\mathbf{u}\cdot\nabla T=\nabla\cdot\kappa\nabla T \tag{4}$$

$$\frac{\partial\overline{\rho S}}{\partial t}=\rho_\mathrm{l}\left[\frac{(\rho_\mathrm{S}-\rho_\mathrm{l})}{\rho_\mathrm{l}}S_\mathrm{l}\frac{\partial\phi}{\partial t}+\mathbf{u}\cdot\nabla S_\mathrm{l}-D\nabla\cdot\phi\nabla S_\mathrm{l}\right] \tag{5}$$

In the above equations,

$$\overline{\rho c}_p=\rho_\mathrm{S}c_{p\mathrm{S}}(1-\phi)+\rho_\mathrm{l}c_{p\mathrm{l}}\phi \tag{6}$$

DOI: 10.1002/fld

and

$$\overline{\rho S}=\rho_S S_S(1-\phi)+\rho_l S_l \phi \tag{7}$$

are the average local heat capacity and average local solute mass concentration in the mushy zone. c_{p_S} and c_{p_l} are the specific heat in the solid and fluid, respectively, T is the temperature, L is the latent heat at the reference temperature T_H, S_S is the solute concentration in the solid and κ is the conductivity.

It is further assumed that there is no undercooling in the mushy zone; hence, the liquidus temperature is a function of the local composition and given by

$$T=mS_l+T_m \tag{8}$$

where the liquidus line in the phase diagram is assumed to be a straight line with slope m and T_m is the melting temperature of the pure solvent. Finally, in the case of no diffusion in the solid the solute concentration in the solid is given by

$$S_S=\frac{1}{1-\phi}\int_{\phi}^{1} kS_l \,\mathrm{d}\phi \tag{9}$$

where k is the partition coefficient assumed to be constant.

The following section addresses the solution to the momentum equation using a projection method, the continuity and momentum equations are expressed in the non-dimensional form to simplify the development. This is accomplished using a reference length H, a reference velocity $U=\sqrt{\beta_S g S_0 H}$ and a reference time $\tau=H/U$. The non-dimensional temperature is given as $T=(T'-T_0)/GH$ and the solute concentration by $S=S'/S_0$, where the prime denotes a dimensional variable. The continuity and momentum equations take the form

$$\nabla\cdot\mathbf{u}=\beta\frac{\partial\phi}{\partial t} \tag{10}$$

$$\begin{aligned}\frac{\partial\mathbf{u}}{\partial t}+\frac{1}{\phi}\mathbf{u}\cdot\nabla\mathbf{u}-\frac{\beta}{\phi}\frac{\partial\phi}{\partial t}\mathbf{u}={}&-\phi\nabla p+\frac{1}{Re}\left(\nabla^2\mathbf{u}+\frac{\beta}{3}\nabla\frac{\partial\phi}{\partial t}\right)-\frac{\phi}{Re}\mathbf{Da}^{-1}\mathbf{u}\\&+\phi\left[\frac{1}{Fr}T+(\operatorname{sign}\beta_S)(S_l-1)\right]\hat{\mathbf{g}}\end{aligned} \tag{11}$$

where $\beta=(\rho_S-\rho_l)/\rho_l$ is the contraction coefficient; the Reynolds number Re, the Froude number Fr and the Darcy tensor $\mathbf{Da}$ are given by

$$Re=\frac{UH}{\nu}$$

$$Fr=\frac{U^2}{\beta_T g G H^2}$$

$$\mathbf{Da}=\frac{1}{H^2}\mathbf{K}$$

G is the initial temperature gradient, and $\hat{\mathbf{g}}$ is a unit vector in the direction of gravity. The permeability tensor $\mathbf{K}$ is assumed to be diagonal; the values have been obtained by means of regression analysis of available empirical data and from numerical calculations for the range of permeability where empirical data cannot be obtained [47–49]. The permeability is given below as a function of the volume fraction of liquid ϕ and the primary dendrite arm spacing d_1,

$$K_{xx}=K_{yy}=\begin{cases} 1.09\times10^{-3}\phi^{3.32}d_1^2, & \phi\leqslant0.65\\ 4.04\times10^{-6}\left[\dfrac{\phi}{1-\phi}\right]^{6.7336}d_1^2, & 0.65<\phi\leqslant0.75\\ \left(-6.49\times10^{-2}+5.43\times10^{-2}\left[\dfrac{\phi}{1-\phi}\right]^{0.25}\right)d_1^2, & 0.75<\phi\leqslant1 \end{cases} \tag{12}$$

$$K_{zz}=\begin{cases} 3.75\times10^{-4}\phi^{2}d_1^2, & \phi\leqslant0.65\\ 2.05\times10^{-7}\left[\dfrac{\phi}{1-\phi}\right]^{10.739}d_1^2, & 0.65<\phi\leqslant0.75\\ 0.074[\log(1-\phi)^{-1}-1.49+2(1-\phi)-0.5(1-\phi)^2]d_1^2, & 0.75<\phi\leqslant1.0 \end{cases} \tag{13}$$

In this work, we consider test calculations in rectangular and parallelepiped geometry only. The initial conditions are one region of all-liquid with no fluid flow, uniform solute concentration and a uniform linear temperature gradient G in the vertical direction. The boundary conditions for the velocity are no-slip and no-normal penetration at solid boundaries; that is the bottom of the container and the vertical walls, and a porous surface at the top to allow flow into the computational region to account for contraction. The side walls are treated as adiabatic, the initial temperature gradient G is imposed at the top, and the bottom surface is cooled at a prescribed rate RC, i.e.

$$T_{\mathrm{b}}(t)=T_{\mathrm{b}}(0)-\mathrm{RC}t \tag{14}$$

where T_{b} denotes the uniform temperature of the bottom surface. For the solute concentration no mass flux is assumed at the bottom and side walls, and a mixed boundary condition is applied at the top so that liquid coming into the region by contraction is at concentration S_0. The computational region for a two-dimensional domain and the boundary conditions are depicted in Figure 1.

4. PROJECTION METHOD

The projection method presented here is based on an approximation that is only first order in time for simplicity. The form of the momentum equation (11) to be satisfied is

$$\frac{\mathbf{u}^{n+1}-\mathbf{u}^{n}}{\Delta t}+\frac{1}{\phi}\mathbf{u}^{n}\cdot\nabla\mathbf{u}^{n}-\frac{\beta}{\phi}\frac{\partial\phi}{\partial t}\mathbf{u}^{n+1}=-\phi\nabla p^{n+1}+\frac{1}{Re}\left(\nabla^2\mathbf{u}^{n}+\frac{\beta}{3}\nabla\frac{\partial\phi}{\partial t}\right)-\frac{\phi}{Re}\mathbf{Da}^{-1}\mathbf{u}^{n+1}$$
$$+\phi\left[\frac{1}{Fr}T^{n+1}+(\operatorname{sign}\beta_{\mathrm{S}})(S_1^{n+1}-1)\right]\hat{\mathbf{g}} \tag{15}$$

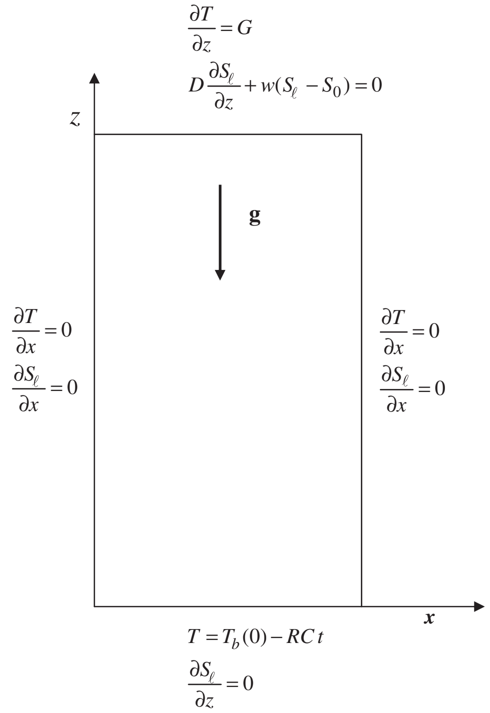
$\frac{\partial T}{\partial z}=G$
$D\frac{\partial S_\ell}{\partial z}+w(S_\ell-S_0)=0$
z
$\mathbf{g}$
$\frac{\partial T}{\partial x}=0$
$\frac{\partial S_\ell}{\partial x}=0$
$\frac{\partial T}{\partial x}=0$
$\frac{\partial S_\ell}{\partial x}=0$
x
$T=T_b(0)-RCt$
$\frac{\partial S_\ell}{\partial z}=0$

Figure 1. Computational domain and boundary conditions in the x–z plane. The same configuration occurs in the y–z plane with the x-derivatives replaced by the y-derivatives along the vertical walls. w denotes the vertical velocity component at the top.

The convective and diffusive terms are treated explicitly. The dependent variables are decomposed in the form

$$\begin{aligned}\mathbf{u}^{n+1}&=\mathbf{u}^*+(\mathbf{u}^{n+1}-\mathbf{u}^*)\\ p^{n+1}&=p^n+(p^{n+1}-p^n)\\ T^{n+1}&=T^n+(T^{n+1}-T^n)\\ S_1^{n+1}&=S_1^n+(S_1^{n+1}-S_1^n)\end{aligned}\tag{16}$$

where $\mathbf{u}^*$ denotes the intermediate velocity in the viscous projection step. Substituting expressions (16) into Equation (15), the latter can be split into the following two expressions:

$$\begin{aligned}&\frac{\mathbf{u}^*-\mathbf{u}^n}{\Delta t}-\frac{\beta}{\phi}\frac{\partial\phi}{\partial t}\mathbf{u}^*+\frac{\phi}{Re}\mathbf{Da}^{-1}\mathbf{u}^*\\ &\quad=-\frac{1}{\phi}\mathbf{u}^n\cdot\nabla\mathbf{u}^n-\phi\nabla p^n\frac{1}{Re}\left(\nabla^2\mathbf{u}^n+\frac{\beta}{3}\nabla\frac{\partial\phi}{\partial t}\right)+\phi\left[\frac{1}{Fr}T^n+(\mathrm{sign}\,\beta_{\mathrm{S}})(S_1^n-1)\right]\hat{\mathbf{g}}\end{aligned}\tag{17}$$

and

$$\frac{\mathbf{u}^{n+1}-\mathbf{u}^*}{\Delta t}-\frac{\beta}{\phi}\frac{\partial\phi}{\partial t}(\mathbf{u^{n+1}}-\mathbf{u}^*)=-\phi\nabla(p^{n+1}-p^n)-\frac{\phi}{Re}\mathbf{Da}^{-1}(\mathbf{u}^{n+1}-\mathbf{u}^*)$$
$$+\phi\left[\frac{1}{Fr}(T^{n+1}-T^n)+(\mathrm{sign}\,\beta_{\mathrm{S}})(S_{\mathrm{l}}^{n+1}-S_{\mathrm{l}}^n)\right]\hat{\mathbf{g}} \qquad (18)$$

From Equation (17) the intermediate velocity is given by

$$\mathbf{u}^*=\left[\left(\frac{1}{\Delta t}-\frac{\beta}{\phi}\frac{\partial\phi}{\partial t}\right)\mathbf{I}+\frac{\phi}{Re}\mathbf{Da}^{-1}\right]^{-1}\left\{\frac{1}{\Delta t}\mathbf{u^n}-\frac{1}{\phi}(\mathbf{u^n}\cdot\nabla)\mathbf{u^n}-\phi\nabla p^n\right.$$
$$\left.+\frac{1}{Re}\left(\nabla^2\mathbf{u}^n+\frac{\beta}{3}\nabla\frac{\partial\phi}{\partial t}\right)+\phi\left[\frac{1}{Fr}T^n+(\mathrm{sign}\,\beta_{\mathrm{S}})(S_{\mathrm{l}}^n-1)\right]\hat{\mathbf{g}}\right\} \qquad (19)$$

The use of a lumped mass matrix makes this calculation explicit, while retaining the Darcy term implicitly. This is essential for the stability and efficiency of the algorithm. Rearranging Equation (18) so that $(\mathbf{u}^{n+1}-\mathbf{u}^*)$ is on its own, and taking the divergence yields

$$-\nabla\cdot\phi\left[\left(\frac{1}{\Delta t}-\frac{\beta}{\phi}\frac{\partial\phi}{\partial t}\right)\mathbf{I}+\frac{\phi}{Re}\mathbf{Da}^{-1}\right]^{-1}\nabla(p^{n+1}-p^n)$$
$$=-\nabla\cdot\mathbf{u}^*+\beta\frac{\partial\phi}{\partial t}-\nabla\cdot\phi\left[\left(\frac{1}{\Delta t}-\frac{\beta}{\phi}\frac{\partial\phi}{\partial t}\right)\mathbf{I}+\frac{\phi}{Re}\mathbf{Da}^{-1}\right]^{-1}$$
$$\times\left[\frac{1}{Fr}(T^{n+1}-T^n)+(\mathrm{sign}\,\beta_{\mathrm{S}})(S_{\mathrm{l}}^{n+1}-S_{\mathrm{l}}^n)\right]\hat{\mathbf{g}} \qquad (20)$$

This is the equation needed to calculate the increment in the pressure, and couples the pressure increment with the changes in the body force term at each time step. The new velocity at time step t_{n+1} is obtained from

$$\mathbf{u}^{n+1}=\mathbf{u}^*-\phi\left[\left(\frac{1}{\Delta t}-\frac{\beta}{\phi}\frac{\partial\phi}{\partial t}\right)\mathbf{I}+\frac{\phi}{Re}\mathbf{Da}^{-1}\right]^{-1}\left\{\nabla(p^{n+1}-p^n)\right.$$
$$\left.-\left[\frac{1}{Fr}(T^{n+1}-T^n)+(\mathrm{sign}\,\beta_{\mathrm{S}})(S_{\mathrm{l}}^{n+1}-S_{\mathrm{l}}^n)\right]\hat{\mathbf{g}}\right\} \qquad (21)$$

It is well known that a variety of issues are associated with the use of projection methods for the solution to the incompressible Navier–Stokes equations. The literature is full of examples, variations on the method and applications to incompressible flow calculations; and many papers are dedicated to estimating its accuracy [27–34]. The general consensus is that the velocity can be determined to second-order accuracy, but there is disagreement on the pressure. Some authors claim that the pressure can be determined to second-order accuracy [30, 50], while others argue that the very nature of the fractional step methods limits the pressure to first-order accuracy no matter what steps are taken to improve the method [51, 52]. However, there is consistent agreement on the necessity to ensure an accurate selection of the boundary conditions for the intermediate velocity [29], accurate selection of the boundary conditions for the pressure [53–55], and the use of appropriate pressure-correction schemes [30, 31, 33, 50]. The first two of these items are related to the inherent difficulty in the fractional step method brought upon by the fact that there is only one real set of boundary conditions for the divergence-free velocity, whereas splitting the solution to the Navier–Stokes equations into two steps requires two sets of boundary conditions. The third item argues for the calculation of the increments in pressure at every time step, relative to the pressure at the previous time step.

Ways to impose boundary conditions on the intermediate velocity have been carefully discussed in [29, 52, 56, 57] and will not be repeated here. Boundary conditions for the pressure Poisson equation are analyzed in [30, 32, 33, 50, 52, 54, 55, 57]; the authors agree that accuracy is improved by the calculation of the incremental pressure, but they do not suggest boundary conditions for the incremental pressure other than to infer that the normal derivatives at the solid boundaries must be homogeneous. In the present implementation the homogeneous Dirichlet boundary conditions are imposed both in the intermediate and the final velocities; the pressure Poisson equation is subjected to homogeneous Neumann boundary conditions everywhere, and the pressure fixed at the upper right corner of the domain.

5. FINITE ELEMENT DISCRETIZATION

The projection method discussed above has been implemented by means of a stabilized finite element formulation based on bi-linear elements with a 2×2 Gauss integration in two dimensions and trilinear elements with a $2\times 2\times 2$ Gauss integration in three dimensions for both the velocity components and the pressure. To avoid locking due to the equal-order interpolation the contributions of the velocity divergence, the pressure and the body force terms are selectively reduced integrated using a one-point Gauss quadrature. This is similar to using a mixed formulation with bilinear velocity and constant element pressure, or a penalty formulation with bilinear velocity. It is known that this element does not satisfy the LBB consistency condition because the consistency constant depends on the mesh parameter h, and the element can lock if the problem data are not smooth [58]. However, except for very rare situations the element converges at the optimal rates of second and first orders for the velocity and pressure, respectively [59]. Furthermore, if selective reduced integration is not applied the method locks as expected. The elements are isoparametric although in the examples shown in this work only rectangular brick shapes are used. A standard Petrov–Galerkin stabilization is applied to the convective terms [60] and lumped mass matrices are used throughout. For further numerical stability considerations, the latent heat term in the temperature equation is re-written in terms of the total solute concentration and temperature in the manner explained in [61]. The calculation of the velocity and solute concentration is done explicitly; however, the diffusion term in the temperature equation is kept implicit requiring the solution to a linear system of equations. The pressure equation is elliptic and also requires an implicit solver. As shown in Equation (15), time has been discretized using a simple backward Euler scheme, the time marching scheme uses a variable time step that is selected for each time step as a function of the maximum velocity in the domain in order to control the stability of the algorithm while maximizing the size of the time step.

6. SIMULATIONS AND DISCUSSION

The projection algorithm was implemented in a three-dimensional solidification simulator that has been used extensively for modeling freckle formation in binary alloys [40]. In the original version published in [40], the momentum equations were solved using a GLS method with equal-order trilinear interpolation for velocity and pressure. This scheme was replaced by the fractional step method presented in Section 3. The same conjugate gradient algorithm with diagonal preconditioning and sparse format storage used in [40] was used in this work to solve the systems of algebraic equations that result from the discretization of the energy and pressure equations.

A Pb–20 wt% Sn alloy was selected for the simulations, which we know from past experience has abundant freckle activity when solidified directionally at low cooling rates. The thermodynamic and transport properties of this alloy are readily available in the literature [12]. A calculation was done in a rectangular region of cross section $10\,\mathrm{mm}\times 10\,\mathrm{mm}$ and of height 20,mm. It is assumed that the alloy fills the domain completely and is enclosed by solid walls; therefore, no-slip boundary conditions are applied on all surfaces. Initially, the alloy is all-liquid with a linear temperature distribution varying from 524 K (slightly larger than the liquidus temperature) at the bottom and 544 K at the top (i.e. a gradient of 1000 K/m). The lateral surfaces are insulated and the initial temperature gradient is imposed at the top. The melt is then directionally solidified from below by prescribing a cooling rate of $\mathrm{RC}=0.5\,\mathrm{K/min}$ on the bottom surface. For simplicity, in these calculations it was assumed that $\rho_{\mathrm{S}}=\rho_{\mathrm{l}}$ and that the domain is completely enclosed.

Several simulations with various meshes were performed to assess the model and the mesh sensitivity of the results. A direct comparison between the results using the different meshes cannot be made, because the number and location of the channels varies from one simulation to another. However, the general trends are as expected and in agreement with the results of the mesh sensitivity study presented in [38].

A simulation was performed with the uniform finite element mesh of trilinear 'brick' elements used in [37], which consists of 40×40 elements in the horizontal cross section and 111 elements in the vertical direction, giving a total of 177 600 elements and 188 272 nodes. This is a much finer resolution than the one used in [40], which had only 12 000 elements in a domain of the same dimensions. This simulation was also attempted with the model used in [40]; it ran for some 100 time steps before encountering convergence difficulties. This is not unusual since the model requires a readjustment of the stabilization parameters as the calculations progress. The CPU time per second of solidification required by this program was 4 times larger than for the model presented here. Furthermore, while a GLS implementation with this mesh takes approximately 650 MB of memory, the present formulation requires only 20 MB. This is because in the GLS formulation, the resulting momentum matrix has 4 degrees of freedom per node (the three velocity components and pressure), while in the fractional step algorithm only the pressure equation (1 degree of freedom per node) must be solved implicitly.

Simulation results after 20 min of solidification are shown in Figures 2–4. The mushy zone has advanced approximately 8 mm and it displays an intense channel activity. A total of 11 channels are observed, which will become freckles after solidification. All the phenomena related to channel-type convection and freckle segregation that were amply described in [40] are also observed here, including the volcano shape of the channel mouths at the tip of the mushy zone, from which plumes of Sn-enriched liquid emerge. Compared with the simulations in [40], however, the channels in the present simulations are observed to penetrate deeper into the mushy zone while still being completely liquid. This is a consequence of the finer mesh in this simulation which can better capture the channel geometry. Figure 4 shows the structure of the channels by plotting the isosurface corresponding to the fraction of liquid$=$0.98. The top of the mushy zone was set semitransparent to better observe the channel positions. Superimposed to this plot, the velocity vectors are shown in regions where the total concentration of Sn is larger than 20.5 wt%. The color

DOI: 10.1002/fld

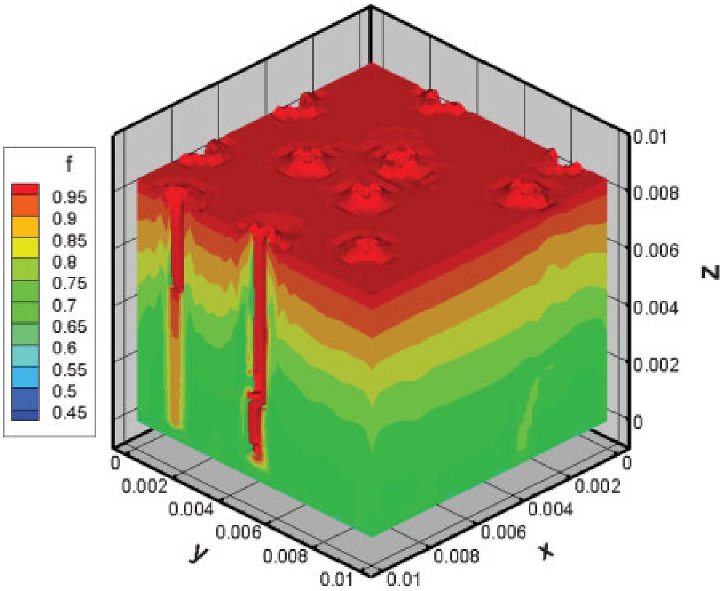

Figure 2. Volume fraction of liquid after 20 min of solidification of Pb–20 wt% Sn alloy, showing channel formation and enhanced growth at channel exits on top of the mushy zone.

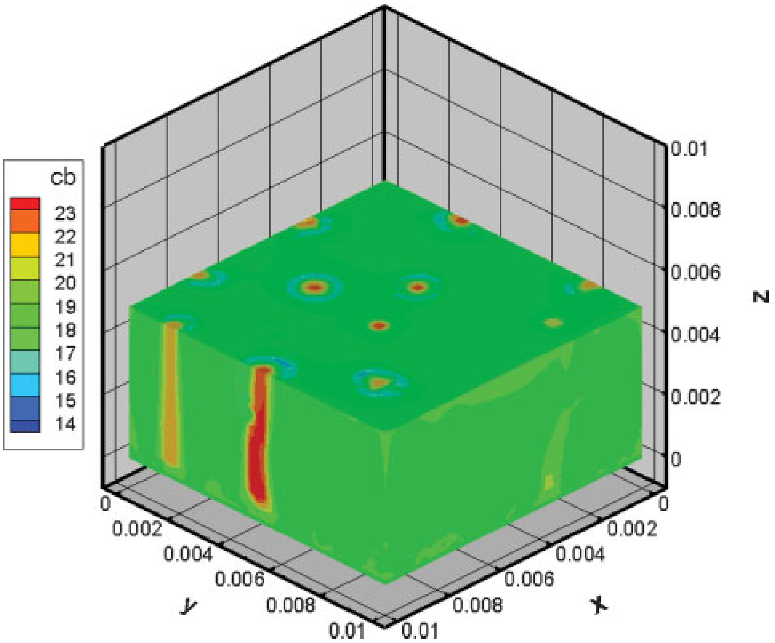

Figure 3. Contours of total mixture concentration (wt%) in the first 5 mm of the mushy zone, showing Sn-enriched liquid inside the channels and depleted Sn around them.

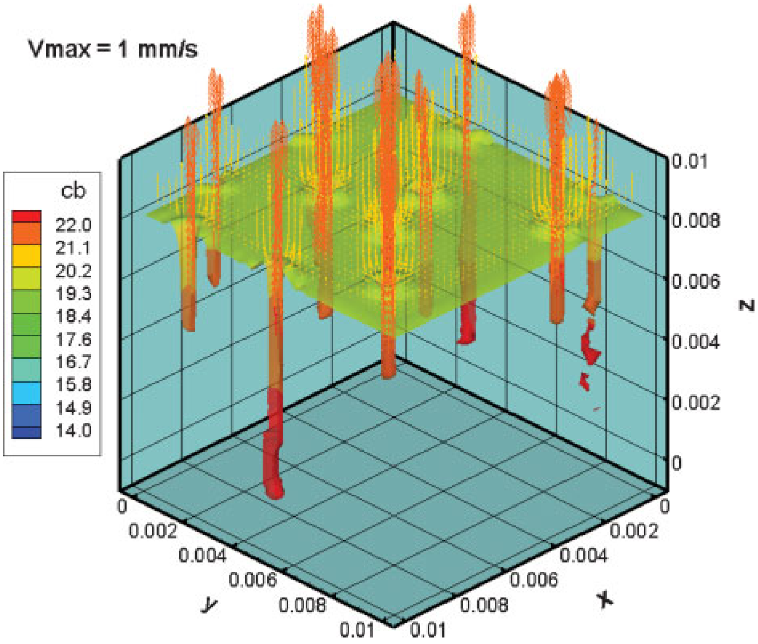

Figure 4. Isosurface $\phi = 0.98$ showing top of the mushy zone and channel structure. Velocity vectors in regions of enriched liquid show plume-type convection. Coloring corresponds to the total concentration of Sn (wt%).

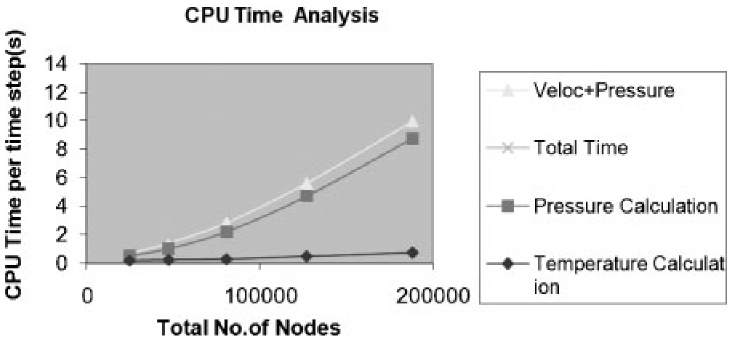

Figure 5. Processor time consumed by different sections of the solidification model as a function of mesh size.

of both the isosurface and the velocity vectors corresponds to the local concentration of Sn. This enables observation of the plume-type convection of Sn-enriched liquid coming out of the channel mouths as well as the re-entrance of less-enriched liquid feeding the sides of the volcano-type structures. The maximum velocity in the domain is approximately 1 mm/s, similar to the values reported in our previous work.

DOI: 10.1002/fld

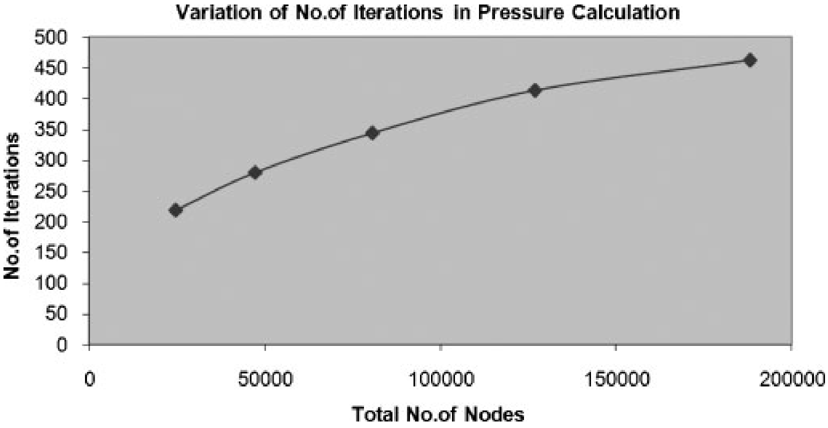

Figure 6. Number of iterations required to solve the pressure equation as a function of mesh size.

The reader is referred to previous publications [12, 40, 41] for extensive details on freckle formation and channel dynamics, which will not be repeated here. Here we discuss the performance of the projection method for this type of calculation. The simulation shown in Figures 2–4 took approximately 4 min of computer time (CPU time) per second of solidification when executed in a DELL XPS 420 PC with one processor of 2.4 GHz. In older hardware (laptop with Pentium-M of 1.7 MHz), the same simulation takes about 10 min per second of solidification. This is a very significant improvement over previously reported performances.

To better understand the performance of the program, CPU time and memory requirements as a function of the problem size were calculated. Figure 5 shows a CPU time analysis, describing the time taken by the separate sections as a function of the mesh size. It is observed that the momentum equation requires about 90% of the CPU time, and the energy equation accounts for less than 10% of the total CPU time, even though both the temperature and pressure equations generate algebraic systems of the same order. Momentum and energy are both solved with the same conjugate gradient solver; this is well known to computational fluid dynamics practitioners. Figure 5 shows that the difference in the CPU time required to solve the pressure and the temperature equations increases significantly with the problem size, and the solution to the pressure accounts for about 75% of the total CPU time. This can be understood by observing Figure 6, which shows the number of iterations as a function of the number of nodes in the mesh required by the conjugate gradient method to solve for the pressure, and how this number increases with mesh refinement. On the other hand, the temperature equation requires around 20 iterations increasing only modestly with the problem size. The efficiency of the pressure solver can be greatly enhanced introducing more sophisticated techniques based on Newton-Krylov or multi-grid preconditioned solvers [62–65].

Even though no effort has been given to the optimization of the projection algorithm, the performance observed in the simulations is highly attractive; it improves by an order of magnitude on previously published results. Combined with parallelization and a more sophisticated pressure solver this algorithm will provide a tool to perform very large, realistic simulations of solidification of castings that so far have been lacking, and that are badly needed for cast design.

DOI: 10.1002/fld

ACKNOWLEDGEMENTS

The authors would like to thank the National Aeronautics and Space Administration that supported D. G. W., many thanks also to Prof. David R. Poirier who has provided insightful comments and invaluable discussions. U. K. S. and S. D. F. appreciate the support of the National Science Foundation under grant number CTS-0553570.

REFERENCES

1. Flemings MC, Nereo GE. Macrosegregation: part I. *Transactions of the Metallurgical Society of AIME* 1967; **239**:1449–1461.
2. Flemings MC, Nereo GE. Macrosegregation: part II. *Transactions of the Metallurgical Society of AIME* 1968; **242**:41–49.
3. Flemings MC, Nereo GE. Macrosegregation: part III. *Transactions of the Metallurgical Society of AIME* 1968; **242**:50–55.
4. Mehrabian R, Keane M, Flemings MC. Interdendritic fluid flow and macrosegregation: influence of gravity. *Metallurgical Transactions* 1970; **1**:1209–1220.
5. Kou S, Poirier DR, Flemings MC. Macrosegregation in rotated remelted ingots. *Metallurgical Transactions B* 1978; **9**:711–719.
6. Ridder SD, Reyes FC, Chakravorty S, Merhabian R, Nauman JD, Chen JH, Klein HJ. Steady-state segregation and heat flow in ESR. *Metallurgical Transactions B* 1978; **9**:415–425.
7. Fujii T, Poirier DR, Flemings MC. Macrosegregation in a multicomponent low alloy steel. *Metallurgical Transactions B* 1979; **10**:331–339.
8. Ridder SD, Kou S, Mehrabian R. Effect of fluid flow on macrosegregation in axi-symmetric ingots. *Metallurgical Transactions B* 1981; **12**:435–447.
9. Maples AL, Poirier DR. Convection in the two-phase zone of solidifying alloys. *Metallurgical Transactions B* 1984; **15**:163–172.
10. Bennon WD, Incropera FP. A continuum model for momentum, heat and species transport in binary solid–liquid phase change systems—I. Model formulation. *International Journal of Heat and Mass Transfer* 1987; **30**:2161–2170.
11. Bennon WD, Incropera FP. A continuum model for momentum, heat and species transport in binary solid–liquid phase change systems—II; applications to solidification in a rectangular cavity. *International Journal of Heat and Mass Transfer* 1987; **30**:2171–2187.
12. Felicelli SD, Heinrich JC, Poirier DR. Simulation of freckles during vertical solidification of a binary alloy. *Metallurgical Transactions B* 1991; **22**:847–859.
13. Beckermann C, Viskanta R. Mathematical modeling of transport phenomena during solidification. *Applied Mechanics Reviews* 1993; **46**:1–27.
14. Schneider MC, Beckermann C. A numerical study of the combined effects of microsegregation, mushy zone permeability and flow, caused by volume contraction and thermosolutal convection, on macrosegregation and eutectic formation in binary alloy solidification. *International Journal of Heat and Mass Transfer* 1995; **38**:3455–3473.
15. Ganesan S, Poirier DR. Conservation of mass and momentum for the flow of interdendritic liquid during solidification. *Metallurgical Transactions B* 1990; **21**:173–181.
16. Poirier DR, Nandapurkar PJ, Ganesan S. The energy and solute conservation equations for dendritic solidification. *Metallurgical Transactions B* 1991; **22**:889–900.
17. Voller VR, Prakash C. A fixed grid numerical modelling methodology for convection–diffusion mushy region phase-change problems. *International Journal of Heat and Mass Transfer* 1987; **30**:1709–1719.
18. Heinrich JC, Felicelli SD, Poirier DR. Vertical solidification of dendritic binary alloys. *Computer Methods in Applied Mechanics and Engineering* 1991; **89**:435–461.
19. Chiang KC, Tsai HL. Shrinkage-induced fluid flow and domain change in two-dimensional alloy solidification. *International Journal of Heat and Mass Transfer* 1992; **35**:1763–1770.
20. Combeau H, Lesoult G. Simulation of freckles formation and related segregation during directional solidification of metallic alloys. In *Modelling of Casting*, *Welding and Advanced Solidification Processes IV*, Piwonka TS, Voller V, Katgerman L (eds). The Minerals, Metals & Materials Society: Warrendale, PA, 1993; 201–208.

21. Naterer GF. Simultaneous pressure–velocity coupling in the two-phase zone for solidification shrinkage in an open casting. *Modelling and Simulation in Materials Science and Engineering* 1997; **5**:595–613.
22. Ahmad N, Combeau H, Desbiolles J-L, Jalanti T, Lesoult G, Rappaz J, Rappaz M, Stomp C. Numerical simulation of macrosegregation: a comparison between finite volume method and finite element method predictions and a confrontation with experiments. *Metallurgical and Materials Transactions A* 1998; **29**:617–630.
23. Zabaras N, Samanta D. A stabilized volume-averaging finite element method for flow in porous media and binary alloy solidification processes. *International Journal for Numerical Methods in Engineering* 2004; **60**:1103–1138.
24. Voller VR, Swaminathan CR, Thomas BG. Fixed grid techniques for phase change problems: a review. *International Journal for Numerical Methods in Engineering* 1990; **30**:875–898.
25. Beckermann C. Modeling of macrosegregation: applications and future needs. *International Materials Reviews* 2002; **47**:243–261.
26. Heinrich JC, Poirier DR. Convection modeling in directional solidification. *Comptes Rendus Mecanique* 2004; **332**:429–445.
27. Chorin AJ. Numerical solution of the Navier–Stokes equations. *Mathematics of Computation* 1968; **22**:745–762.
28. Temam R. Sur l'approximation de la solution des equations de Navier–Stokes par la method de fractionnaires II. *Archive for Rational Mechanics and Analysis* 1969; **33**:377–385.
29. Kim J, Moin P. Application of a fractional-step method to incompressible Navier–Stokes. *Journal of Computational Physics* 1985; **59**:308–323.
30. Bell JB, Collela P, Glaz HM. A second-order projection method for the incompressible Navier–Stokes equations. *Journal of Computational Physics* 1989; **85**:257–283.
31. Gresho PM, Chan ST. On the theory of semi-implicit projection methods for viscous incompressible flow and its implementation via a finite element method that also introduces a nearly consistent mass matrix. Part 2: implementation. *International Journal for Numerical Methods in Fluids* 1990; **11**:621–659.
32. Shen J. On error estimates of projection methods for Navier–Stokes equations: first order schemes. *SIAM Journal on Numerical Analysis* 1992; **29**:258–268.
33. Quartapelle L. *Numerical Solution of the Incompressible Navier–Stokes Equations*. Birkhauser Verlag: Berlin, 1993.
34. Almgren AS, Bell JB, Szymczak WG. A numerical method for the incompressible Navier–Stokes equations based on an approximate projection method. *SIAM Journal on Scientific Computing* 1996; **17**:358–369.
35. Amberg G. Computation of macrosegregation in an iron–carbon cast. *International Journal of Heat and Mass Transfer* 1991; **34**:217–227.
36. Xu D, Li Q. Numerical method for solution of strongly coupled binary alloy solidification problems. *Numerical Heat Transfer A* 1991; **20**:181–201.
37. Westra DG. Simulation of directional solidification in a binary alloy using the fractional step method. *Ph.D. Dissertation*, Department of Aerospace and Mechanical Engineering, The University of Arizona, 2003.
38. Sung PK, Poirier DR, Felicelli SD. Sensitivity of mesh spacing on simulating macrosegregation during directional solidification of a superalloy. *International Journal for Numerical Methods in Fluids* 2001; **35**:357–370.
39. Nielsen DG, Incropera FP. Three-dimensional considerations of unidirectional solidification in a binary liquid. *Numerical Heat Transfer A* 1993; **23**:1–20.
40. Felicelli SD, Heinrich JC, Poirier DR. Three-dimensional simulations of freckles in binary alloys. *Journal of Crystal Growth* 1997; **191**:879–888.
41. Felicelli SD, Poirier DR, Heinrich JC. Modeling freckle formation in three dimensions during solidification of multicomponent alloys. *Metallurgical and Materials Transactions B* 1998; **29**:847–855.
42. Guo J, Beckermann C. Three-dimensional simulation of freckle formation during binary alloy solidification: effect of mesh spacing. *Numerical Heat Transfer A* 2003; **44**:559–576.
43. Samanta D, Zabaras N. Modeling convection in solidification processes using stabilized finite element techniques. *International Journal for Numerical Methods in Engineering* 2005; **60**:1–25.
44. Sabau AS, Viswanathan S. Microporosity prediction in aluminum alloy castings. *Metallurgical and Materials Transactions B* 2002; **33**:243–255.
45. Voller VR, Porté-Agel F. Moore's law and numerical modeling. *Journal of Computational Physics* 2002; **179**: 698–703.
46. Heinrich JC, Poirier DR. The effect of volume change during directional solidification of binary alloys. *Modelling and Simulation in Materials Science and Engineering* 2004; **12**:881–899.
47. Poirier DR. Permeability for flow of interdendritic liquid in columnar-dendritic alloys. *Metallurgical Transactions B* 1987; **18**:245–255.

DOI: 10.1002/fld

48. Ganesan S, Chan CL, Poirier DR. Permeability of flow parallel to dendrite arms. *Materials Science and Engineering A* 1992; **151**:97–105.
49. Bhat MS, Poirier DR, Heinrich JC. Permeability for cross flow through columnar-dendritic alloys. *Metallurgical and Materials Transactions B* 1995; **26**:1049–1056.
50. Van Kan J. A second-order accurate pressure-correction scheme for viscous incompressible flow. *SIAM Journal on Scientific and Statistical Computing* 1986; **7**:870–891.
51. Perot JB. An analysis of the fractional step method. *Journal of Computational Physics* 1993; **108**:51–58.
52. Strikwerda JC, Lee YS. The accuracy of the fractional-step method. *SIAM Journal on Numerical Analysis* 1999; **37**:37–47.
53. Orzag SA, Israeli M, Deville MO. Boundary conditions for incompressible flows. *Journal of Scientific Computing* 1986; **1**:75–110.
54. Weinan E, Liu J-G. Projection method I: convergence and numerical boundary layers. *SIAM Journal on Numerical Analysis* 1995; **32**:1017–1057.
55. Weinan E, Liu J-G. Projection method II: Godunov–Ryabenki analysis. *SIAM Journal on Numerical Analysis* 1996; **33**:1597–1621.
56. Le Veque RL, Oliger J. Numerical analysis project. *Report NA-81-16*, Computer Science Department, Stanford University, Stanford, CA, 1981.
57. Shen J. On error estimates for some higher order projection and penalty-projection methods for the Navier–Stokes equations. *Numerische Mathematik* 1992; **62**:49–73.
58. Carey GF, Oden JT. *Finite Elements*, *Vol. IV*: *Fluid Mechanics*. Prentice-Hall: Englewood Cliffs, NJ, 1986.
59. Carey GF, Krishnan R. Penalty finite element method for the Navier–Stokes equations. *Computer Methods in Applied Mechanics and Engineering* 1984; **42**:183–244.
60. Heinrich JC, Pepper DW. *Intermediate Finite Element Method. Fluid Flow and Heat Transfer Applications*. Taylor & Francis: Philadelphia, PA, 1999.
61. Felicelli SD, Heinrich JC, Poirier DR. Numerical model for dendritic solidification of binary alloys. *Numerical Heat Transfer B* 1993; **23**:461–481.
62. Meister A. Comparison of different Krylov subspace methods embedded in an implicit finite volume scheme for the computation of viscous and inviscid flow fields on unstructured grids. *Journal of Computational Physics* 1998; **140**:311–345.
63. Briggs WL, Henson VE, McCormick SF. *A Multigrid Tutorial* (2nd edn). SIAM: Philadelphia, PA, 2000.
64. Saad Y. *Iterative Methods for Sparse Linear Systems* (2nd edn). SIAM: Philadelphia, PA, 2003.
65. Knoll D, Keyes D. Jacobian-free Newton–Krylov methods: a survey of approaches and applications. *Journal of Computational Physics* 2004; **193**:357–397.

DOI: 10.1002/fld